nature catalysis

ARTICLES

https://doi.org/10.1038/s41929-018-0171-9

Operando NAP-XPS unveils differences in MoO_3 and Mo_2C during hydrodeoxygenation

Karthick Murugappan[1], Eric M. Anderson[1], Detre Teschner[2,3], Travis E. Jones[2], Katarzyna Skorupska[2,3] and Yuriy Román-Leshkov[1*]

MoO_3 and Mo_2C have emerged as remarkable catalysts for the selective hydrodeoxygenation (HDO) of a wide range of oxygenates at low temperatures (that is, ≤673 K) and H_2 pressures (that is, ≤1 bar). Although both catalysts can selectively cleave C–O bonds, the nature of their active sites remains unclear. Here we used operando near-ambient pressure X-ray photoelectron spectroscopy to reveal important differences in the Mo 3*d* oxidation states between the two catalysts during the hydrodeoxygenation of anisole. This technique revealed that, although both catalysts featured a surface oxycarbidic phase, the oxygen content and the underlying phase of the material impacted the reactivity and product selectivity during the hydrodeoxygenation. MoO_3 transitioned between 5+ and 6+ oxidation states during the operation, consistent with an oxygen-vacancy driven mechanism wherein the oxygenate is activated at undercoordinated Mo sites. In contrast, Mo_2C showed negligible oxidation state changes during hydrodeoxygenation and maintained mostly 2+ states throughout the reaction.

Hydrodeoxygenation (HDO) is an important upgrading strategy to convert lignocellulosic biomass into fuels and chemicals that relies on molecular H_2 to remove oxygen selectively in the form of water[1–13]. Although noble metal catalysts have dominated the HDO landscape, molybdenum trioxide (MoO_3) (refs [14–20]) and molybdenum carbide (Mo_2C) (refs [21–31]) recently emerged as promising earth-abundant alternatives that can selectively cleave C–O bonds under mild conditions. In contrast to the state-of-the-art noble metal catalysts, MoO_3 and Mo_2C catalysts produce unsaturated hydrocarbons and concurrently minimize both the saturation of C=C double bonds and the cleavage of C–C bonds.

Román-Leshkov and co-workers showed that MoO_3 converts a wide-range of linear and aromatic oxygenates into olefinic and aromatic hydrocarbons, respectively, with high selectivities (>97%) using low H_2 pressures (≤1 bar) and temperatures below 673 K (ref. [14]). Postreaction characterization studies revealed that MoO_3 underwent partial carburization to form an oxycarbohydride ($MoO_xC_yH_z$) that featured a large proportion of Mo^{5+} surface species[15]. It was hypothesized that these undercoordinated species (that is, oxygen vacancies) were responsible for activating the C–O bond and that the lattice carbon in $MoO_xC_yH_z$ played a crucial role in preventing the over-reduction of Mo^{5+} into less active Mo^{4+} sites[15].

In parallel, Bhan and co-workers showed that Mo_2C is highly selective for cleaving strong phenolic C–O bonds at atmospheric H_2 pressures and temperatures that range from 420 to 553 K (refs [22,23,26,28,29]). For instance, Mo_2C converted anisole into benzene with selectivity values >90% at 423 K. Detailed kinetic studies revealed that two distinct sites are required: one for H_2 dissociative adsorption and one for oxygenate activation[22,26,29]. The site required for oxygenate adsorption was hypothesized to be metal-like in nature, based on the invariant product generation rates when normalized by ex situ CO chemisorption[22,26]. In a subsequent study, an oxygen mass balance performed during transient HDO experiments revealed an oxygen incorporation equivalent to ~0.29 monolayers[27]. Given the lack of bulk structural changes, this oxidation was hypothesized to be a surface and/or a subsurface phenomenon[26–29].

Notwithstanding this evidence, the exact nature of the active sites in both materials remains unresolved. On the one hand, the presence of oxycarbidic sites may suggest a common HDO pathway for both materials. Indeed, although CO chemisorption is typically used to titrate metallic sites that may be present in Mo_2C and not in MoO_3, CO can also bind to the undercoordinated sites of $MoO_xC_yH_z$ (ref. [27]). Hence, the potential active site for oxygenate adsorption in Mo_2C could be either metallic or an oxygen vacancy similar to that observed over MoO_3. On the other hand, reactivity data have shown different HDO product distributions for both materials when compared at identical conditions (Supplementary Fig. 1), which suggests different site speciation over the catalytic surfaces.

Unfortunately, ex situ characterization techniques do not allow us to establish clear structure–performance relationships for these materials. Although postreaction X-ray photoelectron spectroscopy (XPS) of spent MoO_3 provided insights into the nature of the catalysts after reaction, this ex situ approach does not capture the dynamics of the catalyst surface under the reaction conditions[32]. More importantly, Mo_2C is highly oxophilic and readily forms an oxide passivation layer when exposed to O_2 (refs ([33–35]). This changes the surface structure from that present during the reaction and convolutes data from ex situ characterization methods[34]. As both catalysts undergo significant structural and surface modifications during the course of the reaction, an in situ surface characterization technique is required to interrogate the active sites responsible for HDO.

Here we used operando near-ambient pressure XPS (NAP-XPS) to probe the nature of active sites over MoO_3 and Mo_2C catalysts during the HDO of anisole at 593 K and H_2 pressures ≤1 mbar. Using synchrotron radiation, we were able to increase the surface sensitivity by modulating the incident photon energies to measure ejected photoelectrons at lower kinetic energies than those measured with traditional ultra-high vacuum XPS[32]. Our study revealed

[1]Department of Chemical Engineering, Massachusetts Institute of Technology, Cambridge, Massachusetts, USA. [2]Fritz-Haber-Institut der Max-Planck-Gesellschaft, Abteilung Anorganische Chemie, Berlin, Germany. [3]Max-Planck-Institut für Chemische Energiekonversion, Mülheim a. d. Ruhr, Germany. *e-mail: yroman@mit.edu

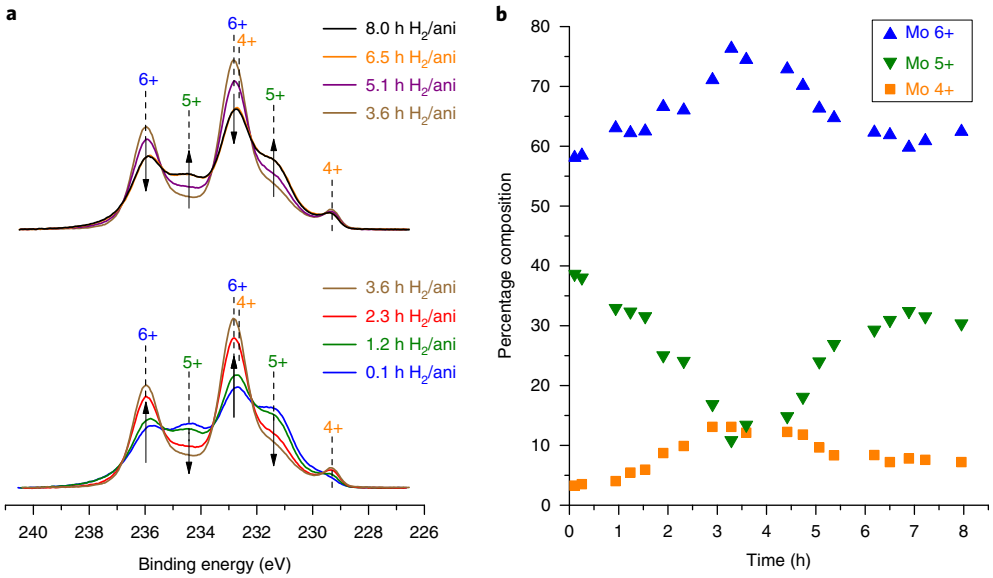

Fig. 1 | NAP-XPS of prereduced MoO_3 during the HDO of anisole at a photon energy of 473 eV. a, Normalized Mo 3*d* spectra at selected (for better visualization) time points from the entire data set. **b**, Percent composition of Mo oxidation states with time. Reaction conditions: $T = 593$ K, $P_{total} = 1$ mbar ($P_{anisole} = 0.005$ mbar, balance H_2). ani: anisole.

that both catalysts predominantly produced benzene as the major product under the reaction conditions investigated. However, the changes in Mo 3*d* oxidation states during HDO were drastically different across both materials. The Mo 3*d* core-level spectra were rigorously analysed with the aid of density functional theory (DFT) calculations to identify the various contributions associated with different chemical environments. In addition to Mo 3*d* spectra, O 1*s*, C 1*s*, surface elemental composition and C/Mo and O/Mo ratios were examined to gain insight into the cause of deactivation. Thus, our work provides a robust framework to interpret Mo 3*d* XPS data for MoO_3 and Mo_2C catalysts.

Results

NAP-XPS measurements. To investigate the nature of the active sites during HDO, NAP-XPS measurements were performed over both MoO_3 and Mo_2C samples under identical reaction conditions (Fig. 1). Due to the lack of reliable fitting strategies for surface-sensitive Mo 3*d* spectra for Mo_2C, DFT calculations were used to aid in developing a robust fit parameter set. In short, we benchmarked our theoretical approach first by simulating known Mo 3*d* line shapes of metallic Mo and MoO_2 and then by calculating the line shape of Mo_2C (Supplementary Methods I, Supplementary Fig. 2 and Supplementary Table 1).

Figure 1a shows the Mo 3*d* XPS spectra acquired over prereduced MoO_3 during the reaction. Detailed information about Mo 3*d* binding energies, deconvolution parameters and a sample deconvoluted spectrum are available in Supplementary Methods II, Supplementary Tables 1–3, and Supplementary Fig. 3. In the first 3.6 h, there was a clear continuous oxidation of Mo^{5+} to Mo^{6+}, as seen by the lower intensities of Mo^{5+} peaks and the sharper Mo^{6+} peaks in Fig. 1a. Interestingly, after about four hours on stream, the proportion of Mo^{6+} started to decline with a concomitant increase of Mo^{5+}, and ultimately reached a steady state. No peaks that corresponded to Mo^{2+} (Mo_2C) or Mo (Mo metal) were observed. The distribution of Mo oxidation states was tracked as a function of time (Fig. 1b). Specifically, the proportion of Mo oxidation states changed from 39% Mo^{5+} and 58% Mo^{6+} to 11% Mo^{5+} and 76% Mo^{6+} in the first 3.3 h, before reaching a steady-state distribution of 31% Mo^{5+} and 61% Mo^{6+}. Similarly, Mo^{4+} mirrored the trends observed with Mo^{6+}, increasing from ~3% to 13% in the first 3.3 h, before decreasing to a steady-state composition of ~8% Mo^{4+} species. A repeat of the experiment with a new MoO_3 pellet resulted in similar trends (Supplementary Figs. 6–8).

Control experiments on fresh MoO_3 samples were used to gain insights into the observed changes in Mo oxidation states during the HDO. First, the Mo 3*d* spectra of untreated MoO_3 (that is, not pretreated with H_2) acquired at 593 K in 1 mbar N_2 flow predominantly featured a combination of Mo^{6+} and Mo^{5+} states with their respective $3d_{5/2}$ peaks located at 232.8 eV (ref. [36]) and 231.5 eV (ref. [36–38]) (Supplementary Fig. 9). The presence of Mo^{5+} species indicates that the sample underwent a partial thermal reduction. Bulk MoO_2 (Supplementary Fig. 10) featured oxidation states that correspond to Mo^{4+} (52%), with additional contributions from the Mo^{5+} (23%) and Mo^{6+} states (25%). Although most reports typically model Mo^{4+} as one set of doublet peaks[38,39], recent surface science literature shows that Mo^{4+} actually consists of two pairs of doublets with one narrow, asymmetric pair associated with a screened metallic environment, and one broader, more symmetric pair that corresponds to an unscreened environment[40–42]. Here we also associated the Mo^{4+} state with two sets of doublets with their Mo $3d_{5/2}$ peaks located at ~229.3 and 230.6 eV. Next, a prereduced MoO_3 sample exposed to only H_2 gas (that is, in the absence of anisole) at 593 K showed a decreasing proportion of Mo^{6+} species from ~67% to 61% with a concomitant increase in Mo^{5+} from ~32% to 38% in the first 2.2 h, before approaching a steady-state distribution of ~36% Mo^{5+} and 62% Mo^{6+} thereafter (Supplementary Figs. 11 and 12).

The HDO of anisole was investigated over Mo_2C after it was treated for three hours with H_2 at 593 K (Supplementary Fig. 13). This prereduction was necessary to remove any surface oxides formed during the sample handling and loading prereaction (vide infra). In stark contrast to the Mo 3*d* spectra of prereduced MoO_3, no significant changes were observed in the Mo oxidation states over Mo_2C during the course of the HDO reaction (Fig. 2a). The distribution of Mo species remained relatively constant at ~84% Mo^{2+}, 14% Mo^{4+}, 1% Mo^{5+} and 1% Mo^{6+} (Fig. 2b) throughout the reaction (about seven hours), and resembled that obtained after the H_2 reduction. A repeat experiment with a new Mo_2C pellet showed similar trends (Supplementary Figs. 14–17). A control experiment

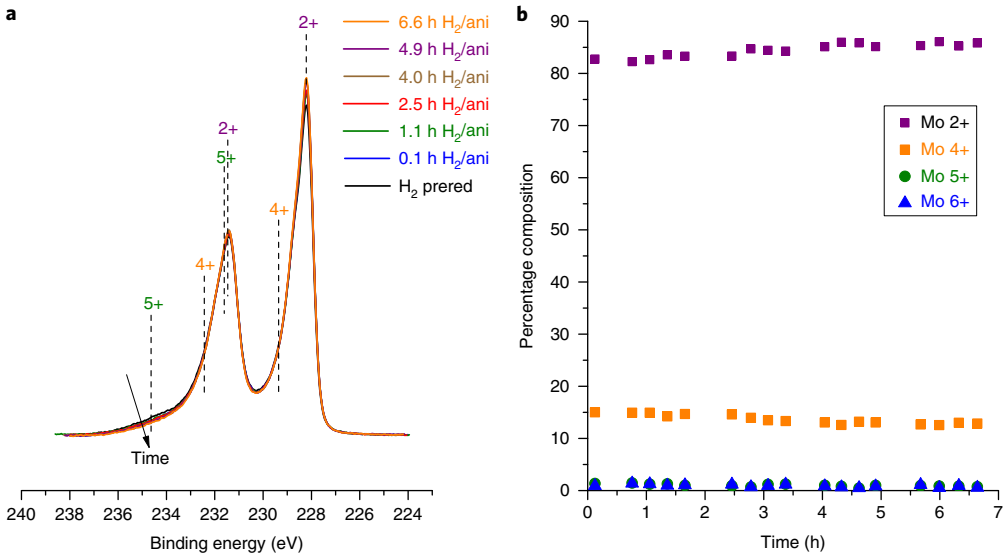

Fig. 2 | NAP-XPS of Mo_2C during the HDO of anisole at a photon energy of 473 eV. a, Normalized Mo 3*d* spectra at selected (for better visualization) time points from the entire data set. **b**, Percent composition of Mo oxidation states with time. Reaction conditions: $T = 593$ K, $P_{total} = 1$ mbar ($P_{anisole} = 0.005$ mbar, balance H_2) and H_2 prereduction (prered) = 3 h. ani: anisole.

with fresh Mo_2C in the presence of just H_2 (that is, in the absence of anisole) was performed prior to the HDO experiment to determine the Mo 3*d* binding energies that correspond to Mo_2C. The corresponding Mo 3*d* binding energies, deconvolution fit parameters and a representative deconvoluted spectrum for Mo_2C are given in Supplementary Methods II, Supplementary Tables 1, 4 and 5 and Supplementary Fig. 4. Although most reports associate Mo^{2+} in Mo_2C with a single set of doublets, our theoretical analysis (Supplementary Fig. 2) showed that Mo^{2+} features three sets of doublets. The dominant doublet, which corresponds to Mo^{2+}, is strongly asymmetric in nature and corresponds to the Mo $3d_{5/2}$ signal at 228.2 eV (Supplementary Fig. 18a), in agreement with prior literature reports[43,44]. In addition, two minor doublets with their Mo $3d_{5/2}$ bands centred at ~228.9 and 231.9 eV also correspond to Mo^{2+} (Supplementary Fig. 4). Despite our attempts to minimize air exposure, a ~0.33 nm thick oxide overlayer (Supplementary Methods III and Supplementary Table 6) exists on the 'fresh' Mo_2C surface, as evidenced by the presence of a broad shoulder in the Mo 3*d* spectra at higher binding energies. Peak deconvolution revealed that ~72% of the Mo species exist as Mo^{2+}, associated with carbidic Mo_2C, and Mo^{4+}, Mo^{5+} and Mo^{6+} constitute the remaining 15%, 10% and 3%, respectively, associated with oxidic species. We note that a conservative Mo_2C fitting was performed wherein the asymmetry parameter of the dominant Mo^{2+} peak was not allowed to be too high to obtain reasonable fits, and thus potentially underestimate the Mo^{2+} and overestimate the higher oxide contributions. The presence of residual oxygen on freshly synthesized Mo_2C was also observed by Chen and Bhan[29]. The intense carbidic C 1*s* signal at ~283.1 eV (refs [45–47]) is a strong indication that the surface is carbidic or oxycarbidic in nature (Supplementary Fig. 18b). In addition, a signal at 284.5 eV associated with graphitic carbon[43], and peaks at 285.9 and 288.1 eV, which correspond to the oxidized carbon entities C–O (ref. [48]) and C=O, respectively) are also visible in the spectrum. As seen from Supplementary Fig. 19, maintaining the catalyst under H_2 flow at 593 K decreased the oxide layer on the surface, but did not completely eliminate it. Specifically, the amount of Mo^{2+} increased by ~10% after three hours under H_2 flow, and appeared to remain relatively constant at this value thereafter. As such, a three-hour prereduction was performed before the HDO reaction. The invariance in amount of Mo^{2+} after three hours suggests that the remaining oxide layer (which corresponds to Mo^{4+}, Mo^{5+} and Mo^{6+} species) on the carbide is probably more difficult to remove under these mild reduction conditions, consistent with prior reports wherein temperatures above 823 K were required to remove the residual oxygen from fresh Mo_2C catalysts[29].

Micro-gas chromatography (micro-GC) results. Benzene was the major HDO product observed over both MoO_3 (Supplementary Fig. 20) and Mo_2C (Supplementary Fig. 21). However, the rates of benzene formation were very different. On the introduction of the H_2-anisole saturated stream over prereduced MoO_3, the benzene concentration increased sharply to reach a maximum in 1.3 h, before very slowly decreasing over the next 6.7 h (Supplementary Fig. 20). In contrast, over Mo_2C, the benzene concentration reached a maximum in just ~0.4 h, before dropping rapidly in the next 2.5 h (Supplementary Fig. 21). The benzene content continued to decrease thereafter, albeit at a slower rate. The presence of two deactivation profiles over Mo_2C is also consistent with the observations from anisole HDO experiments performed at 593 K and atmospheric H_2 pressures over bulk and supported Mo_2C (Supplementary Figs. 22 and 23). Notably, Mo_2C generated almost an order of magnitude more benzene than MoO_3, which suggests that although both catalysts produced benzene, Mo_2C was significantly more active than MoO_3 under similar reaction conditions. We note that, although Mo_2C (~25 $m^2 g^{-1}$) has a higher Brunauer–Emmett–Teller surface area than MoO_3 (~5 $m^2 g^{-1}$) before reaction, Delporte et al. showed that the surface area of MoO_3 increased from 4 $m^2 g^{-1}$ to 150 $m^2 g^{-1}$ over 15 hours in the presence of either H_2 or a H_2/hydrocarbon mixture at 623 K (ref. [49]). Our catalyst probably undergoes a similar increase in surface in the presence of a H_2/anisole mixture, although the extent of such an increase is uncertain because the total pressure employed was significantly lower (1 mbar). Normalizing the rate by the prereaction surface area (that is, a higher bound for MoO_3) still indicated that Mo_2C is a more active HDO catalyst than MoO_3. Minor products typically observed during the anisole HDO at 593 K and 1.013 bar of H_2 over MoO_3, such as phenol, cresols, toluene and methane, were not observed during the NAP-XPS experiments ($P_{H_2} < 0.001$ bar)[15]. As the H_2 pressure employed in this study is three orders of magnitude lower than that used under typical reactivity studies, the generation of these minor products prob-

ably falls below the detection limit of the micro-GC detector. As expected, benzene was the dominant product over Mo_2C, consistent with the high benzene selectivity (≥94% selectivity on a C_6^+ basis) observed during the anisole HDO at 593 K and 1 bar H_2 pressure. This value is slightly higher than that observed by Bhan and co-workers during anisole HDO at 150 °C (refs [26,27]) and this difference can be attributed to the absence of cyclohexane formed from the sequential hydrogenation of benzene at 593 K. Thermodynamic calculations show that benzene hydrogenation to give cyclohexane is unfavourable ($\Delta G_{reaction} = +16.69\,kJ\,mol^{-1}$) at 593 K (Supplementary Table 11)[50,51]. However, as no cyclohexane was detected, the calculated approach to equilibrium (Supplementary Table 11) was probably much smaller than 1, which thus indicates that benzene hydrogenation was not thermodynamically limited but probably kinetically controlled[26,51]. This low hydrogenation rate suggests a suppressed hydrogenation activity of the oxygen-modified Mo_2C catalyst, as previously observed in the presence of oxygenated reactants such as anisole and other lignin-derived aromatics[26,28]. The direct HDO of anisole over Mo_2C typically yields benzene and methanol, with the latter undergoing further HDO to form methane and water[26]. However, no peaks that correspond to methane or methanol were observed in this study, probably due to the low amounts produced, which approached the detection limit of the micro-GC (10 ppm).

Powder X-ray diffraction (PXRD). PXRD patterns of the prereduced MoO_3 showed that the bulk MoO_3 structure was preserved during the three-hour H_2 pretreatment (Supplementary Fig. 24). Similarly, the PXRD pattern of fresh Mo_2C showed only peaks associated with β-Mo_2C, with no visible diffractions from MoO_2 (Supplementary Fig. 25). PXRD patterns of spent MoO_3 catalysts did not show any appreciable changes in the bulk MoO_3 structure (Supplementary Fig. 26). No new peaks that corresponded to $MoO_xC_yH_z$ or MoO_2 were observed, contrasting to the PXRD patterns observed after the HDO of *m*-cresol at 593 K (ref. [15]). This can be attributed to the significantly lower H_2 pressure employed here, which might not be high enough to cause a bulk transformation of the catalyst. Although bulk oxycarbide was not observed after the reaction, the increased presence of Mo^{5+} observed at the surface is indicative of surface oxycarbide formation (vide infra), consistent with our previous studies[15]. Similarly, PXRD patterns of spent Mo_2C catalysts (Supplementary Fig. 27) revealed that the bulk structure of Mo_2C was preserved during the HDO reaction, in agreement with prior observations by Bhan and co-workers[26].

Discussion

Mo 3*d* spectra acquired during the HDO of anisole over prereduced MoO_3 across both replicate experiments featured an initial oxidation phase (about four hours) followed by a reduction phase before approaching a steady-state composition. Effectively, the catalyst underwent an initial transient oxidation–reduction cycle to move closer to its working state, as seen by the relatively constant distribution of Mo species towards the end of the experiment. During the initial stages of the reaction, the anisole feed oxidized the Mo^{5+} surface species to Mo^{6+} species, even at the high H_2/anisole molar ratios (~215) used. Similarly, the proportion of Mo^{4+} first increased, which implies that some Mo sites were over-reduced to Mo^{4+} during the prereduction before reaching a steady value of ~8%. This smaller proportion of Mo^{4+} on the surface compared to that for the Mo^{5+} or Mo^{6+} states indicates that Mo^{4+} does not play a significant role in HDO. We note that the amount of Mo^{4+} observed during these experiments was significantly lower than that observed in our prior work (49% Mo^{4+})[16], probably due to the slower rate of reduction at the lower H_2 pressures used in the NAP-XPS chamber. We also note that no oxidation was observed in the control experiments with MoO_3 in the absence of feed (anisole), which rules out any significant oxygen contamination in the chamber. As the oxidation was only observed on introduction of the feed, this is probably a direct effect from the interaction of the oxygenate with the catalyst surface. Once the feed is introduced, oxygen from the anisole can bind favourably to the undercoordinated Mo sites (Mo^{5+}), and thereby oxidize the Mo species. This result is in line with observations by Delporte et al. wherein carbon atoms from the reactant rapidly fill oxygen vacancies to form an oxycarbohydride phase, and thereby prevent the formation of MoO_2 (ref. [49]). Similarly, our previous work also revealed that prereduced MoO_3 transformed into a mixture of $MoO_xC_yH_z$ and MoO_2 after coming into contact with *m*-cresol for 0.5 h (ref. [15]). In this study, oxidation continued up to about four hours, at which point the catalyst transitioned to its working state with an equilibrated ratio of Mo^{6+}/Mo^{5+} and steady-state HDO rates. This oxidation–reduction cycle could possibly depict the actual turnovers observed on the MoO_3 catalytic surface. Taken together, the interplay of the Mo^{5+} and Mo^{6+} states is strong evidence that Mo^{5+} is active for HDO under these reaction conditions. Furthermore, Mo 3*d* spectra acquired at higher photon energies of 946 eV and 1,486.7 eV (Supplementary Figs. 28–30) revealed that the surface of MoO_3 featured more Mo^{5+} and fewer Mo^{6+} states than the bulk, and thus further confirmed that Mo^{5+} is the active site responsible for the HDO over MoO_3. The adsorption of oxygenates onto such undercoordinated Mo sites is also consistent with mechanisms proposed during the HDO of acrolein[52] and acetaldehyde[53] over MoO_3. Similarly, the same depth-profile analysis (Supplementary Figs. 29 and 30) showed that the bulk was more enriched with the Mo^{4+} states than the surface and that the amount of Mo^{4+} in the bulk increased during the reaction, which indicates a bulk-like over-reduction, that is, the transport of oxygen vacancies propagating down to the bulk. This observation is also consistent with the rapid deactivation observed over MoO_3 at 673 K during the HDO of *m*-cresol, attributed to the complete bulk reduction of MoO_3 to MoO_2 (Mo^{4+})[15], which indicates that Mo^{4+} is not that active for HDO.

Analysis of the Mo 3*d* spectra of Mo_2C revealed that the dominant Mo^{2+} phase was maintained throughout the reaction and shows negligible oxidation even in the presence of the oxygenate feed. We note that the H_2 prereduction, as expected, led to an initial increase in the Mo^{2+} content (from 72 to 83%) and a corresponding decrease in the oxide overlayer thickness (from 0.33 to 0.20 nm (Supplementary Table 6)). However, both the composition of the Mo oxidation states and the oxygen coverage did not vary significantly during the HDO reaction, similar to that reported by Schaidle et al. during the HDO of acetic acid over Mo_2C (ref. [54]). The prevalence of the Mo^{2+} species and the negligible changes in the Mo^{5+}/Mo^{6+} oxidation states imply that the dominant carbide/oxycarbide phase is probably responsible for the HDO over Mo_2C. This presence of an oxycarbide phase during the HDO was also illustrated by Schaidle et al. using DFT calculations, wherein a submonolayer of oxygen was shown to exist on the Mo–Mo_2C(001) and C–Mo_2C(001) surfaces during the HDO of acetic acid[54]. Using a combination of in situ diffuse reflectance infrared Fourier transform spectroscopy, temperature-programmed desorption of ammonia and DFT calculations, a 0.50 monolayer of O/C–Mo_2C(001) was proposed as the likely active catalyst surface under the reaction conditions investigated in their study[54].

Based on Mo_2C's nearly invariant Mo 3*d* spectra, in situ oxidation probably cannot account for the observed catalyst deactivation. Bhan and co-workers attributed the catalyst deactivation both to mild coke formation and to in situ oxidation[27]. If in situ oxidation was a major cause of deactivation, the proportion of higher Mo oxidation states (that is, Mo^{4+}, Mo^{5+} and Mo^{6+}) would have increased with a concurrent decrease in the presence of Mo^{2+} species. Furthermore, XPS of the spent supported Mo_2C catalysts (performed using an air-free transfer vessel with ultrahigh vacuum XPS) after the HDO of anisole at 593 K, 1 bar H_2, also revealed that the dominant Mo^{2+} state was maintained during the reaction even after 24 hours with

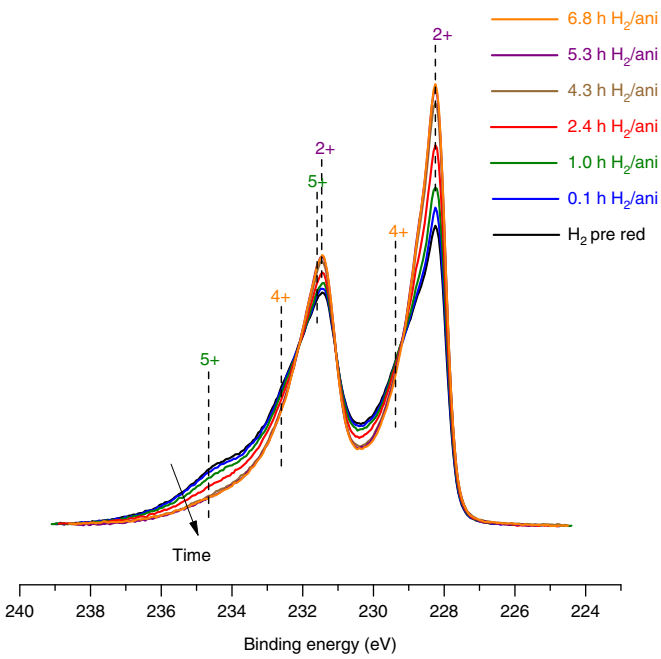

Fig. 3 | Normalized Mo 3*d* spectra of Mo_2C-pass during the HDO of anisole measured at a photon energy of 473 eV. Reaction conditions: $T = 593$ K, $P_{total} = 1$ mbar ($P_{anisole} = 0.005$ mbar, balance H_2) and H_2 prereduction (prered) = 3 h. ani: anisole.

no appreciable surface oxidation (Supplementary Fig. 31), which excluded in situ oxidation as a cause for the observed deactivation, even for the atmospheric H_2 experiments. However, the O 1*s* spectra featured a signal at ~532.7 eV (Supplementary Figs. 32 and 33) that can be attributed to the oxygen present in anisole-derived reaction intermediates or to methoxy species on the catalyst surface[26,55]. The signal increased during the reaction, which implies a growing oxygenate adsorption that potentially leads to deactivation by blocking some of the sites. Although this increase is also consistent with the oxygen incorporation reported by Bhan and co-workers[27], it seems to be a minor effect as it did not change the relative ratio of Mo oxidation states or the O/Mo ratios (Supplementary Figs. 34 and 35), as reported by Schaidle et al.[54]. It is possible that the rates of oxygen incorporation and surface reduction could have reached equilibrium, and thereby led to minimal changes on the quantity of O on the surface measured by XPS. This result is in agreement with prior reports wherein in situ oxidation predominantly occurred during the transient phase of the HDO and that no further oxygen incorporation was observed during the steady-state HDO[27]. Similarly, as 'fresh' Mo_2C already had some oxygen on the surface prior to the reaction (about a 0.20 nm oxide overlayer), only minute amounts of oxygen were likely incorporated during the reaction. Hence, although in situ oxidation cannot be excluded as a cause for the deactivation observed in this study, it probably plays only a minor role in the overall decrease in catalyst performance.

The role of coking in catalyst deactivation was investigated by analysing the C 1*s* spectra, the surface elemental composition and the C/Mo atomic ratios. The time-resolved C 1*s* spectra and the composition of different C 1*s* components showed no significant changes (Supplementary Figs. 37–39), which suggests that the nature of the surface carbon species was largely invariant throughout the reaction. However, surface elemental quantification (Supplementary Methods IV) revealed that the C content increased by ~6% (Supplementary Fig. 40). Similarly, the atomic C/Mo ratio as measured by XPS (Supplementary Fig. 41) increased by ~14%, which indicates a growing amount of carbonaceous deposits on the surface during the course of the reaction. The rise in both the surface concentration of atomic carbon and the C/Mo ratios across duplicate experiments (Supplementary Figs. 42–44) is in agreement with the observations by Bhan and co-workers[27] and Schaidle et al.[54]. Taken together, these data are strong evidence that coking is probably the major cause of the deactivation route for Mo_2C under the reaction conditions investigated here.

To understand the effect of an oxygen overlayer on the carbide surface on the HDO reactivity, a passivated carbide (Mo_2C-pass) was investigated under identical reaction conditions. The passivation oxide overlayer on Mo_2C-pass was determined to be approximately 1.34 nm, roughly four times thicker than that observed over fresh Mo_2C. High Mo oxidation states dominated the Mo 3*d* spectra of the Mo_2C-pass (Supplementary Fig. 45), with only a small contribution from Mo^{2+} (20% of the Mo surface species), which is significantly lower than that for fresh Mo_2C (72%). The C 1*s* spectrum shows a carbidic signal at 283.2 eV, albeit less intense than that observed with fresh Mo_2C (Supplementary Fig. 46). The signals at 285.9 and 288.1 eV, associated with oxidized carbon, are stronger than those of fresh Mo_2C. Supplementary Fig. 47 shows that the passivated layer is partially reduced during the H_2 treatment, as seen by an increase in the fraction of Mo^{2+} from 20% to 55% and a corresponding decrease in oxygen coverage to about a 0.57 nm oxide overlayer or roughly 1.8 monolayers (based on a Mo–O bond distance of 0.318 nm (ref. [56])), similar to the 1.3 monolayers observed by Bhan and co-workers on a Mo_2C-pass catalyst after H_2 treatment[27].

The anisole feed did not further oxidize the Mo species on Mo_2C-pass (Fig. 3). In fact, the oxide layer continued to decrease in intensity during the reaction. Supplementary Fig. 48 shows that the combined proportion of Mo^{4+}, Mo^{5+} and Mo^{6+} decreased from ~45% to 27% during the reaction in the first four hours, and the amount of Mo^{2+} concurrently increased from ~55% to 73%. The composition of the Mo species was relatively constant after this four-hour period, analogous to the trend observed with fresh Mo_2C. Similarly, the oxygen coverage further decreased to a 0.27 nm oxide overlayer, which approaches the oxygen coverage values observed over fresh Mo_2C after the HDO reaction. Interestingly, although the Mo_2C-pass sample showed similar amounts of reactivity towards benzene production (Supplementary Fig. 49) compared to fresh Mo_2C, this material also generated small quantities of toluene. This alkylation product is typically observed on bulk MoO_3 (refs. [14,15]) and is also a minor alkylation product observed on H_2-activated Mo_2C-pass during the HDO of anisole[26]. The presence of toluene indicates that the surface of the Mo_2C-pass features Brønsted acidity[51], consistent with previous reports[54,57]. The presence of acid sites on Mo_2C is dependent on many factors, such as the carburization conditions, passivation treatment, oxygen removal efficiency during the H_2 prereduction and the presence of oxygen co-feed or any other oxygenates during reaction. Sullivan et al. used 2,6-di-*tert*-butylpyridine titrations to reveal that Brønsted acid sites were responsible for the dehydration of isopropanol to propylene over an oxygen-modified Mo_2C and that these acid site densities can be reversibly tuned by a factor of ~30 using an O_2 co-feed[58]. Furthermore, Baddour *et al.* showed that the proportion of acid sites can be tuned by the phase/composition of Mo_2C and the acid strength itself can be varied by the carbide particle size[59]. In summary, acid sites can be either found inherently on Mo_2C or can be formed during pretreatment or during the reaction. However, the significance of these acid sites with respect to controlling reactivity is reaction dependent. In the reaction investigated in our study, as anisole does not have an sp^3-hybridized β-hydrogen, it cannot undergo dehydration, which thus leads to deoxygenation mechanisms different from those observed during dehydration in the above-mentioned studies. The O 1*s* and C 1*s* spectra, as well as the elemental surface composition of carbon and atomic C/Mo ratios, also showed similar trends

to those observed with fresh Mo_2C (Supplementary Figs. 50–53). Mo_2C-pass featured a single deactivation regime (Supplementary Fig. 49), in comparison to the two deactivation zones observed over fresh Mo_2C. Overall, these differences in reactivity over fresh Mo_2C and Mo_2C-pass can be explained by the different amounts of initial oxides present on their surfaces. Specifically, the formation of toluene suggests that when the carbide passivation layer is thicker, the sites on the surface behave more like those in the bulk oxide material. Although toluene production in this study was below the detection limit due to the lower HDO reactivity of MoO_3 at these conditions, alkylation activity was reported for the bulk[14,15] and supported MoO_3 (ref. [20]) catalysts when operating at higher reactant partial pressures.

Although NAP-XPS showed that both MoO_3 and Mo_2C had surface oxycarbidic ($Mo_xO_yC_z$) features, the oxycarbide observed over MoO_3 was significantly richer in oxygen than that on the surface of Mo_2C. As shown in Fig. 1, the Mo oxidation states observed for the oxycarbide present on MoO_3 transition between the +6 and +5 oxidation states during the reaction. In contrast, the oxycarbide over Mo_2C shows almost no +6 or +5 oxidation states and ~15% +4 oxidation state without a change in the course of HDO (Fig. 2). This stark difference implies that the active sites of the two catalysts must be different. In addition to the differences in oxygen content, the electronic structure of the oxycarbide is altered by the MoO_3 or Mo_2C underlayer, which in turn affects the HDO activity. Differences in the surface composition of the catalysts manifest as differences in reactivity, selectivity and catalyst stability.

To verify these differences, HDO experiments of 4-methylanisole were performed in flow reactors over Mo_2C and MoO_3 catalysts supported on silica (Supplementary Methods V). Supported catalysts were used for these studies to mitigate differences in the surface areas generated from formation of the oxycarbide phase. HDO performed with Mo_2C/SiO_2 at 5 bar H_2 and 623 K resulted in a complete conversion of 4-methylanisole with a selectivity to toluene of ~90%, consistent with the high benzene selectivity observed in the HDO of anisole (Supplementary Fig. 55). Under identical reaction conditions and similar space velocities, MoO_3/SiO_2 converted 15% of 4-methylanisole with an initial selectivity to toluene of ~80% that reduced to ~60% after 14 hours, and remained constant at this value thereafter (Supplementary Fig. 56). Additionally, a combined selectivity to oxygenates, which comprised mostly *p*-cresol, dimethylanisole and dimethylphenol, at a steady state of approximately 30% was observed. The presence of dimethylanisole and dimethylphenol also confirmed the presence of Brønsted acid sites capable of catalysing alkylation. In contrast, a negligible transalkylation activity was observed for Mo_2C, consistent with the high selectivity to C–O bond cleavage and minimal alkylation observed in previous reports[26–28]. Comparing MoO_3 with Mo_2C, it is apparent that oxycarbide generated from Mo_2C is more reactive and selective for HDO than the oxycarbide on MoO_3 under identical reaction conditions.

Mo_2C also showed excellent stability as it maintained 40% of its initial activity even after 140 hours on stream (Supplementary Fig. 55). The deactivation profiles obtained across two experiments were identical with first-order deactivation rate constants of 0.017 h^{-1}. We hypothesize that the higher H_2 pressures employed in these experiments both reduced the formation of carbonaceous deposits and aided in the faster removal of coke already formed on the catalyst surface. To investigate this hypothesis, a series of reactions were performed over fresh Mo_2C catalyst in which the H_2 pressure was varied from 1 to 6 bar (Supplementary Fig. 57). The first-order deactivation rate constants were plotted against the average methane selectivity for the respective reaction conditions (Supplementary Fig. 58). A lower deactivation rate constant correlated with a higher methane selectivity, which implies that larger amounts of carbonaceous deposits were removed as methane at higher H_2 pressures, thereby significantly increased the catalyst stability. This deactivation mode is consistent with the higher C/Mo ratios observed by NAP-XPS over the carbide material during the reaction.

In summary, both MoO_3 and Mo_2C are promising HDO catalysts, capable of converting biomass-based oxygenate molecules into more valuable fuels and chemicals. Both catalysts were investigated for the HDO of anisole at 1 mbar and 593 K by the concurrent measurement of the Mo 3*d*, O 1*s* and C 1*s* spectra. MoO_3 and Mo_2C produced benzene as the main HDO product. Mo 3*d* spectra for the prereduced MoO_3 showed that Mo^{5+} was initially oxidized to give Mo^{6+}, followed by reduction to regenerate Mo^{5+} during the course of the HDO reaction. In contrast, the Mo 3*d* spectra of fresh Mo_2C revealed that the dominant carbide phase (Mo^{2+}) was retained throughout the HDO reaction, with no significant changes in the distribution of surface Mo species, which also included a small proportion of surface oxide species (~0.20 nm overlayer). The carbide materials appeared to deactivate mainly via coking. An experiment with Mo_2C-pass generated toluene in addition to benzene, which demonstrates that the presence of oxide moieties generates acid sites sufficiently strong to promote alkylation.

Overall, our findings are largely consistent with the observations of Bhan and co-workers[27], wherein the dominant carbide phase is associated with a highly selective HDO product. Although the surface of fresh Mo_2C is predominantly carbidic in nature (~85% Mo^{2+}) throughout the reaction, it still has some oxidic character (~15% total of Mo^{4+}, Mo^{5+} and Mo^{6+}). This observation suggests that the high HDO selectivity over Mo_2C can be attributed to some adsorbed oxygen on the Mo_2C surface[26], which results in the formation of just benzene from anisole. Taken together, NAP-XPS experiments over Mo_2C and Mo_2C-pass reveal that surface oxygen is probably necessary for selective HDO, but that too much surface oxygen makes the catalyst behave more like MoO_3, which results in the production of alkylation side products. Hence, controlling the surface oxygen concentration on the surface oxycarbidic phase is critical to the control of HDO reactivity and product selectivity.

Methods

Preparation of materials. Anisole (99%) was used as the reactant, and purchased from VWR International. Bulk MoO_3 (≥99.5%) and molybdenum oxide (MoO_2 (≥99%)) were purchased from Sigma-Aldrich. Bulk MoO_3 was prereduced for 3 h at 593 K and 1.013 bar under a H_2 flow (70 ml min^{-1}) to generate undercoordinated sites and remove the induction period reported in our previous study[15]. Prereduced MoO_3 was transferred to the glove box and sealed in a vial to prevent any oxidation. Fresh Mo_2C was synthesized from ammonium paramolybdate tetra(para)hydrate ($(NH_4)_6Mo_7O_{24}{\cdot}4H_2O$ (99%, Alfa Aesar)) using a temperature-programmed reaction method. Ammonium paramolybdate was loaded into a ¼ inch (6.35 mm) U-tube reactor, dispersed on top of a quartz wool plug, in contact with a K-type thermocouple (Omega, TJ36-CAXL-116u). The reactor was then placed in a furnace (Carbolite, GTF 11/50/750B) connected to a temperature controller (Digi-Sense, 68900-10). Ammonium paramolybdate tetra(para) hydrate was heated in a 21% CH_4/H_2 mixture (70 ml min^{-1} total flow) from room temperature to 923 K at 3 K min^{-1} and held at 923 K for 1 h. The resulting sample (Mo_2C) was then held under pure H_2 flow (55 ml min^{-1}) at 923 K for another hour to scavenge residual surface carbon. The sample was cooled down under H_2 flow to room temperature. This U-tube reactor was equipped with valves for the isolation of the catalyst to prevent any exposure to air. Once room temperature was reached, the U-tube was then transferred to a nitrogen-filled glove box and the resulting Mo_2C catalyst was transferred to a 5 ml borosilicate glass ampoule (Wheaton) and capped with a septum. These ampoules were then evacuated on a Schlenk line outside the glove box, before being flame sealed. Mo_2C-pass was prepared under similar carburization conditions in a tube furnace, before being passivated with a 1% O_2/N_2 mixture for 2 h and then being exposed to the ambient atmosphere.

PXRD. PXRD was performed on a Bruker D8 diffractometer using nickel-filtered Cu Kα radiation ($\lambda = 1.5418$ Å). PXRD patterns were acquired on a two-dimensional image plate and rotated at 15 revolutions per minute for 2θ values that ranged from 20 to 90° with a step size of 0.04° and a scan speed of 0.2 s per step.

NAP-XPS experiments. NAP-XPS experiments were performed at the Innovative Station for In Situ Spectroscopy end station of the BESSY II synchrotron facility in Berlin, Germany[32]. The set-up consisted of a differentially

pumped electrostatic lens system and a SPECS hemispherical electron analyser. A detailed explanation of the set-up is given elsewhere[32]. To ensure an equal surface sensitivity, Mo 3*d*, O 1*s* and C 1*s* core-level regions were recorded using selected photon energies such that the ejected photoelectrons had a similar kinetic energy (~245 eV) across the different elements. This kinetic energy corresponds to a 0.66 nm inelastic mean free path (IMFP) for Mo_2C and a 0.78 nm IMFP for MoO_3 based on the NIST Electron IMFP Database[60]. Given that the information depth is roughly three times the IMFP value, ~95% of the ejected photoelectrons arise from a depth of ~2.0 and 2.3 nm, approximately the top ten and seven atomic layers of Mo_2C (Mo–C bond of 0.206 nm)[56] and MoO_3 (Mo–O bond of 0.318 nm)[56], respectively. The spot size was 300 μm × 100 μm and the beam was moved to a new spot on the catalyst pellet (vide infra) for every set of XPS spectra measurement to minimize the beam-induced reduction of molybdenum species[41]. XPS spectra were acquired in the normal emission geometry with a pass energy of 20 eV and a step size of 0.05 eV for Mo 3*d* and of 0.1 eV for C 1*s* and O 1*s*. At each time point, the elemental core-level spectra were measured sequentially in this order: Mo 3*d*, C 1*s* and O 1*s*. For each elemental core level, typically 5–8 scans were recorded. In total, the duration of the spectrum acquisition for each elemental core level was ~5 min. All the XPS spectra shown in this article and Supplementary Information correspond to the catalyst state measured at that time point, and the time stamp refers to the start of the Mo 3*d* core-level spectra acquisition. Binding energies for each element were corrected using their respective second-order peaks. After binding energy correction, the spectra were normalized and a Shirley background was applied[61]. The spectra were then deconvoluted by least-square fitting of the Gaussian–Lorentzian profiles using the software Plot[62], with exponential tail contributions added to account for the asymmetry in some of the peaks. DFT calculations were performed for metallic Mo, MoO_2 and Mo_2C to determine the joint density of states from which the theoretical XPS line shapes (Supplementary Fig. 2) were generated to serve as references for the identification of the binding energies of the various constituent contributions for each compound (Supplementary Table 1). Two sets of optimization parameters were determined based on analysing multiple spectra to best fit the MoO_3 and Mo_2C spectra (Supplementary Tables 2–5 and Supplementary Figs. 3 and 4). Then, the same set of parameters was used consistently across the MoO_3 and Mo_2C samples, respectively. The following constraints were used to determine the best optimization parameters: (1) a spin–orbit splitting of 3.15–3.20 eV for Mo $3d_{5/2}$ and $3d_{3/2}$, (2) an area ratio of 3:2 for Mo $3d_{5/2}$:Mo $3d_{3/2}$, and (3) an equal Gaussian–Lorentzian ratio for Mo $3d_{5/2}$ and Mo $3d_{3/2}$. For quantitative elemental analysis, the raw areas for each element were integrated and then normalized by their respective photon flux and photoionization cross-sections and asymmetry parameters (Supplementary Methods IV, Supplementary Tables 7–10 and Supplementary Fig. 5).

Prereduced MoO_3 and fresh Mo_2C catalyst powders were pressed into pellets (7 mm diameter) using a hand-held pellet press (Pike Technologies) in a nitrogen-filled glove box. Fresh MoO_3, MoO_2 and Mo_2C-pass were pelletized in the ambient atmosphere. The catalyst pellet was then placed between two stainless-steel plates, which were then mounted onto a sapphire plate and secured with screws. The temperature was measured using a K-type thermocouple, which was wound around the screws, pressed firmly against the back plate and very close to the catalyst pellet. The air-sensitive pellets were moved from the glove box to the NAP-XPS set-up using a transfer vessel, which was then mounted directly onto the XPS set-up to minimize air exposure. The sample was locally heated using laser irradiation of the unpolished back plate. All the NAP-XPS experiments were typically run at 1 mbar. The gas flows and the pressure of the reaction chamber were regulated using multiple mass flow controllers (MFCs, Bronkhorst) and motorized control valves. The anisole feed was introduced to the reaction chamber using a stainless-steel saturator in the form of a H_2–anisole saturated stream. H_2 gas was initially saturated with anisole in the saturator at room temperature and at 1.013 bar using a MFC set at 30 ml min^{-1}. This corresponds to a H_2/anisole molar ratio of ~215. A part of this flow was delivered to the reaction chamber held at 1 mbar via a low ΔP MFC (17–20 ml min^{-1}). The rest of the saturated gas stream was directed to the vent. All the catalyst samples were heated at 5 K min^{-1} from room temperature to 593 K, and maintained at 593 K throughout the experiments. MoO_3 and MoO_2 were heated in a N_2 flow (10 ml min^{-1}), whereas the Mo_2C catalysts were heated under a H_2 flow (10 ml min^{-1}) before switching to the H_2–anisole mixture (17–20 ml min^{-1}) for all the reactions at 593 K. During reaction, the gas-phase composition was monitored using a four-channel micro-GC (CP-4900, Varian Inc.) equipped with thermal conductivity detectors. The micro-GC consists of four columns—two Molsieve 5 columns (10 m and 20 m), a PoraPLOT Q (PPQ) column (10 m) and an Al_2O_3/KCl column (10 m). The PPQ column was predominantly used to track benzene and anisole. All the columns were held isothermal at the following temperatures: the two Molsieve columns at 328 K and 315 K, the PPQ column at 453 K and the Al_2O_3/KCl column at 423 K. Each micro-GC run lasted for about 7.3 min, before the next injection was made. Typically, when no reactions were run, the anisole-saturated H_2 stream was injected into the micro-GC via a bypass line (10 ml min^{-1}). When the reaction was started, the H_2–anisole mixture was delivered to the reaction chamber with the bypass switched off. Similarly, at the end of each experiment, the H_2–anisole mixture was turned off and the bypass resumed. The bypass served as a baseline reference for the amount of benzene observed in the absence of a reaction.

Data availability

All data are available from the corresponding author upon reasonable request.

Received: 18 December 2017; Accepted: 25 September 2018;
Published online: 05 November 2018

References

1. Furimsky, E. Catalytic hydrodeoxygenation. *Appl. Catal. A* **199**, 147–190 (2000).
2. Huber, G. W., Iborra, S. & Corma, A. Synthesis of transportation fuels from biomass: chemistry, catalysts, and engineering. *Chem. Rev.* **106**, 4044–4098 (2006).
3. Choudhary, T. & Phillips, C. Renewable fuels via catalytic hydrodeoxygenation. *Appl. Catal. A* **397**, 1–12 (2011).
4. Bu, Q. et al. A review of catalytic hydrodeoxygenation of lignin-derived phenols from biomass pyrolysis. *Bioresour. Technol.* **124**, 470–477 (2012).
5. He, Z. & Wang, X. Hydrodeoxygenation of model compounds and catalytic systems for pyrolysis bio-oils upgrading. *Catal. Sustainable Energy* **1**, 28–52 (2012).
6. Ruddy, D. A. et al. Recent advances in heterogeneous catalysts for bio-oil upgrading via 'ex situ catalytic fast pyrolysis': catalyst development through the study of model compounds. *Green Chem.* **16**, 454–490 (2014).
7. Tran, N., Uemura, Y., Chowdhury, S. & Ramli, A. A review of bio-oil upgrading by catalytic hydrodeoxygenation. *Appl. Mech. Mater.* **625**, 255–258 (2014).
8. Saidi, M. et al. Upgrading of lignin-derived bio-oils by catalytic hydrodeoxygenation. *Energy Environ. Sci.* **7**, 103–129 (2014).
9. Schutyser, W. et al. Influence of bio-based solvents on the catalytic reductive fractionation of birch wood. *Green Chem.* **17**, 5035–5045 (2015).
10. Anderson, E. M. et al. Reductive catalytic Fractionation of corn stover lignin. *ACS Sustainable Chem. Eng.* **4**, 6940–6950 (2016).
11. Anderson, E., Crisci, A., Murugappan, K. & Román-Leshkov, Y. Bifunctional molybdenum polyoxometalates for the combined hydrodeoxygenation and alkylation of lignin-derived model phenolics. *ChemSusChem* **10**, 2226–2234 (2017).
12. Venkatakrishnan, V. K., Delgass, W. N., Ribeiro, F. H. & Agrawal, R. Oxygen removal from intact biomass to produce liquid fuel range hydrocarbons via fast-hydropyrolysis and vapor-phase catalytic hydrodeoxygenation. *Green Chem.* **17**, 178–183 (2015).
13. Anderson, E. M. et al. Flowthrough reductive catalytic fractionation of biomass. *Joule* **1**, 613–622 (2017).
14. Prasomsri, T., Nimmanwudipong, T. & Román-Leshkov, Y. Effective hydrodeoxygenation of biomass-derived oxygenates into unsaturated hydrocarbons by MoO_3 using low H_2 pressures. *Energy Environ. Sci.* **6**, 1732–1738 (2013).
15. Prasomsri, T., Shetty, M., Murugappan, K. & Román-Leshkov, Y. Insights into the catalytic activity and surface modification of MoO_3 during the hydrodeoxygenation of lignin-derived model compounds into aromatic hydrocarbons under low hydrogen pressures. *Energy Environ. Sci.* **7**, 2660–2669 (2014).
16. Shetty, M., Murugappan, K., Prasomsri, T., Green, W. H. & Román-Leshkov, Y. Reactivity and stability investigation of supported molybdenum oxide catalysts for the hydrodeoxygenation (HDO) of m-cresol. *J. Catal.* **331**, 86–97 (2015).
17. Murugappan, K. et al. Supported molybdenum oxides as effective catalysts for the catalytic fast pyrolysis of lignocellulosic biomass. *Green Chem.* **18**, 5548–5557 (2016).
18. Zhou, G., Jensen, P. A., Le, D. M., Knudsen, N. O. & Jensen, A. D. Atmospheric hydrodeoxygenation of biomass fast pyrolysis vapor by MoO_3. *ACS Sustainable Chem. Eng.* **4**, 5432–5440 (2016).
19. Nolte, M. W., Zhang, J. & Shanks, B. H. Ex situ hydrodeoxygenation in biomass pyrolysis using molybdenum oxide and low pressure hydrogen. *Green Chem.* **18**, 134–138 (2016).
20. Shetty, M., Murugappan, K., Green, W. H. & Román-Leshkov, Y. Structural properties and reactivity trends of molybdenum oxide catalysts supported on zirconia for the hydrodeoxygenation of anisole. *ACS Sustainable Chem. Eng.* **5**, 5293–5301 (2017).
21. Ren, H. et al. Selective hydrodeoxygenation of biomass-derived oxygenates to unsaturated hydrocarbons using molybdenum carbide catalysts. *ChemSusChem* **6**, 798–801 (2013).
22. Lee, W.-S., Wang, Z., Zheng, W., Vlachos, D. G. & Bhan, A. Vapor phase hydrodeoxygenation of furfural to 2-methylfuran on molybdenum carbide catalysts. *Catal. Sci. Technol.* **4**, 2340–2352 (2014).

23. Xiong, K., Lee, W. S., Bhan, A. & Chen, J. G. Molybdenum carbide as a highly selective deoxygenation catalyst for converting furfural to 2-methylfuran. *ChemSusChem* **7**, 2146–2149 (2014).
24. Xiong, K., Yu, W. & Chen, J. G. Selective deoxygenation of aldehydes and alcohols on molybdenum carbide (Mo_2C) surfaces. *Appl. Surf. Sci.* **323**, 88–95 (2014).
25. McManus, J. R. & Vohs, J. M. Deoxygenation of glycolaldehyde and furfural on Mo_2C/Mo(100). *Surf. Sci.* **630**, 16–21 (2014).
26. Lee, W.-S., Wang, Z., Wu, R. J. & Bhan, A. Selective vapor-phase hydrodeoxygenation of anisole to benzene on molybdenum carbide catalysts. *J. Catal.* **319**, 44–53 (2014).
27. Lee, W.-S., Kumar, A., Wang, Z. & Bhan, A. Chemical titration and transient kinetic studies of site requirements in Mo_2C-catalyzed vapor phase anisole hydrodeoxygenation. *ACS Catal.* **5**, 4104–4114 (2015).
28. Chen, C.-J., Lee, W.-S. & Bhan, A. Mo_2C catalyzed vapor phase hydrodeoxygenation of lignin-derived phenolic compound mixtures to aromatics under ambient pressure. *Appl. Catal. A* **510**, 42–48 (2016).
29. Chen, C.-J. & Bhan, A. Mo_2C Modification by CO_2, H_2O, and O_2: effects of oxygen content and oxygen source on rates and selectivity of *m*-cresol hydrodeoxygenation. *ACS Catal.* **7**, 1113–1122 (2017).
30. He, S., Broom, J., van der Gaast, R. & Seshan, K. Hydro-pyrolysis of lignocellulosic biomass over alumina supported platinum, Mo_2C and WC catalysts. *Front. Chem. Sci. Eng.* **12**, 155–166 (2017).
31. Iida, T. et al. Encapsulation of molybdenum carbide nanoclusters inside zeolite micropores enables synergistic bifunctional catalysis for anisole hydrodeoxygenation. *ACS Catal.* **7**, 8147–8151 (2017).
32. Knop-Gericke, A. et al. X-Ray photoelectron spectroscopy for investigation of heterogeneous catalytic processes. *Adv. Catal.* **52**, 213–272 (2009).
33. Patt, J., Moon, D. J., Phillips, C. & Thompson, L. Molybdenum carbide catalysts for water–gas shift. *Catal. Lett.* **65**, 193–195 (2000).
34. Sullivan, M. M., Chen, C.-J. & Bhan, A. Catalytic deoxygenation on transition metal carbide catalysts. *Catal. Sci. Technol.* **6**, 602–616 (2016).
35. Choi, J.-S., Bugli, G. & Djéga-Mariadassou, G. Influence of the degree of carburization on the density of sites and hydrogenating activity of molybdenum carbides. *J. Catal.* **193**, 238–247 (2000).
36. Song, Z. et al. Molecular level study of the formation and the spread of MoO_3 on Au(111) by scanning tunneling microscopy and X-ray photoelectron spectroscopy. *J. Am. Chem. Soc.* **125**, 8059–8066 (2003).
37. Clayton, C. & Lu, Y. Electrochemical and XPS evidence of the aqueous formation of Mo_2O_5. *Surf. Interface Anal.* **14**, 66–70 (1989).
38. Marin-Flores, O., Scudiero, L. & Ha, S. X-ray diffraction and photoelectron spectroscopy studies of MoO_2 as catalyst for the partial oxidation of isooctane. *Surf. Sci.* **603**, 2327–2332 (2009).
39. Sian, T. S. & Reddy, G. Optical, structural and photoelectron spectroscopic studies on amorphous and crystalline molybdenum oxide thin films. *Sol. Energy Mater. Sol. Cells* **82**, 375–386 (2004).
40. Scanlon, D. O. et al. Theoretical and experimental study of the electronic structures of MoO_3 and MoO_2. *J. Phys. Chem. C* **114**, 4636–4645 (2010).
41. Baltrusaitis, J. et al. Generalized molybdenum oxide surface chemical state XPS determination via informed amorphous sample model. *Appl. Surf. Sci.* **326**, 151–161 (2015).
42. Frank, B., Cotter, T. P., Schuster, M. E., Schlögl, R. & Trunschke, A. Carbon dynamics on the molybdenum carbide surface during catalytic propane dehydrogenation. *Chem. Eur. J.* **19**, 16938–16945 (2013).
43. Oshikawa, K., Nagai, M. & Omi, S. Characterization of molybdenum carbides for methane reforming by TPR, XRD, and XPS. *J. Phys. Chem. B* **105**, 9124–9131 (2001).
44. Ledoux, M. J., Huu, C. P., Guille, J. & Dunlop, H. Compared activities of platinum and high specific surface area Mo_2C and WC catalysts for reforming reactions: I. Catalyst activation and stabilization: reaction of *n*-hexane. *J. Catal.* **134**, 383–398 (1992).
45. Óvári, L., Kiss, J., Farkas, A. P. & Solymosi, F. Reactivity of Mo_2C/Mo(100) toward oxygen: LEIS, AES, and XPS study. *Surf. Sci.* **566**, 1082–1086 (2004).
46. Clair, T. P. S. et al. Surface characterization of α-Mo_2C(0001). *Surf. Sci.* **426**, 187–198 (1999).
47. Sugihara, M., Ozawa, K., Edamoto, K. & Otani, S. Photoelectron spectroscopy study of Mo_2C(0001). *Solid State Commun.* **121**, 1–5 (2001).
48. Gao, Q., Zhao, X., Xiao, Y., Zhao, D. & Cao, M. A mild route to mesoporous Mo_2C–C hybrid nanospheres for high performance lithium-ion batteries. *Nanoscale* **6**, 6151–6157 (2014).
49. Delporte, P., Pham-Huu, C., Vennegues, P., Ledoux, M. J. & Guille, J. Physical characterization of molybdenum oxycarbide catalyst; TEM, XRD and XPS. *Catal. Today* **23**, 251–267 (1995).
50. Janz, G. J. Thermodynamics of the hydrogenation of benzene. *J. Chem. Phys.* **22**, 751–752 (1954).
51. Baddour, F. G. et al. Late-transition-metal-modified β-Mo_2C catalysts for enhanced hydrogenation during guaiacol deoxygenation. *ACS Sustainable Chem. Eng.* **5**, 11433–11439 (2017).
52. Moberg, D. R., Thibodeau, T. J., Amar, F. G. & Frederick, B. G. Mechanism of hydrodeoxygenation of acrolein on a cluster model of MoO_3. *J. Phys. Chem. C* **114**, 13782–13795 (2010).
53. Mei, D., Karim, A. M. & Wang, Y. Density functional theory study of acetaldehyde hydrodeoxygenation on MoO_3. *J. Phys. Chem. C* **115**, 8155–8164 (2011).
54. Schaidle, J. A. et al. Experimental and computational investigation of acetic acid deoxygenation over oxophilic molybdenum carbide: surface chemistry and active site identity. *ACS Catal.* **6**, 1181–1197 (2016).
55. Liang, J. et al. Effective conversion of heteroatomic model compounds in microalgae-based bio-oils to hydrocarbons over β-Mo_2C/CNTs catalyst. *J. Mol. Catal. A* **411**, 95–102 (2016).
56. Lee, J. S., Locatelli, S., Oyama, S. & Boudart, M. Molybdenum carbide catalysts 3. Turnover rates for the hydrogenolysis of *n*-butane. *J. Catal.* **125**, 157–170 (1990).
57. Bej, S. K., Bennett, C. A. & Thompson, L. T. Acid and base characteristics of molybdenum carbide catalysts. *Appl. Catal. A* **250**, 197–208 (2003).
58. Sullivan, M. M., Held, J. T. & Bhan, A. Structure and site evolution of molybdenum carbide catalysts upon exposure to oxygen. *J. Catal.* **326**, 82–91 (2015).
59. Baddour, F. G., Nash, C. P., Schaidle, J. A. & Ruddy, D. A. Synthesis of α-MoC_{1-x} nanoparticles with a surface-modified SBA-15 hard template: determination of structure–function relationships in acetic acid deoxygenation. *Angew. Chem. Int. Ed.* **55**, 9026–9029 (2016).
60. Powel, C. & Jablonski, A. *NIST Electron Inelastic-Mean-Free-Path Database* Version 1.2, SRD 71 (National Institute of Standards and Technology, Gaithersburg, 2010, accessed 24 September 2017).
61. Roiaz, M. et al. Reverse water–gas shift or Sabatier methanation on Ni(110)? Stable surface species at near-ambient pressure. *J. Am. Chem. Soc.* **138**, 4146–4154 (2016).
62. Plot v.0.997 (M. Wesemann & B. J. Thijsse, 2007).

Acknowledgements

This research was funded by BP through the MIT Energy Initiative Advanced Conversion Research Program and the National Science Foundation (award no. 1454299). We thank Helmholtz-Zentrum Berlin for the allocation of synchrotron radiation beam time at the ISISS beamline of BESSY II. T.E.J. acknowledges the Alexander-von-Humboldt Foundation for financial support.

Author contributions

K.M. and Y.R.-L. conceived the research ideas and designed the experiments. K.M. prepared the materials and performed the PXRD. K.M., E.M.A., D.T. and K.S. performed the NAP-XPS experiments. K.M. and D.T. analysed the XPS data. T.E.J. performed the DFT calculations. K.M. and Y.R.-L. co-wrote the paper. Y.R.-L. supervised the project. All the authors discussed the results and commented on the different versions of the manuscript.

Competing interests

The authors declare no competing interests.

Additional information

Supplementary information is available for this paper at https://doi.org/10.1038/s41929-018-0171-9.

Reprints and permissions information is available at www.nature.com/reprints.

Correspondence and requests for materials should be addressed to Y.R.

Publisher's note: Springer Nature remains neutral with regard to jurisdictional claims in published maps and institutional affiliations.